PHYSICAL REVIEW B **110**, 064322 (2024)

Octahedral tilt distortion in negative thermal expansion in the fluorides $CaZrF_6$ and ScF_3

Kaiyue Zhao,[1] Yixin Jiao,[1] Qiang Sun,[1,*] Ri He,[2,†] Andrea Sanson,[3] Zhicheng Zhong,[2] Erjun Liang,[1] and Qilong Gao[1,‡]
[1]*Key Laboratory of Materials Physics of Ministry of Education, and School of Physics and Microelectronics, Zhengzhou University, Zhengzhou 450052, China*
[2]*Key Laboratory of Magnetic Materials Devices and Zhejiang Province Key Laboratory of Magnetic Materials and Application Technology, Ningbo Institute of Materials Technology and Engineering, Chinese Academy of Sciences, Ningbo 315201, China*
[3]*Department of Physics and Astronomy and Department of Management and Engineering, University of Padua, Padova I-35131, Italy*

(Received 21 May 2024; revised 25 July 2024; accepted 9 August 2024; published 26 August 2024)

Understanding the mechanism of negative thermal expansion (NTE) and controlling the thermal expansion properties of materials at the atomistic level have long captured the attention of scholars. In this regard, the NTE mechanism of fluorides such as monometallic ScF_3 and bimetallic fluorides like $CaZrF_6$ is particularly interesting; despite sharing similar crystal structure, $CaZrF_6$ exhibits a thermal expansion coefficient twice that of ScF_3. Why is this so? Here, we investigate the structural vibrations of these two substances in real and reciprocal space at atmospheric and zero pressure, respectively, using machine-learning based deep potentials in combination with density-functional theory. Our study reveals that the structural flexibility of $CaZrF_6$ results in a greater number of vibration modes exhibiting negative Grüneisen parameters. Moreover, the combined impact of octahedral distortion and tilt vibration leads to a substantially greater NTE for $CaZrF_6$ compared to ScF_3. This work offers insights into understanding and tailoring NTE by considering polyhedral distortion in other open-framework materials.

DOI: 10.1103/PhysRevB.110.064322

I. INTRODUCTION

It is widely acknowledged that thermal expansion and mismatches in coefficients of thermal expansion (CTE) in solids can pose significant challenges for devices and instruments [1]. The discovery of compounds exhibiting negative thermal expansion (NTE) opens avenues for addressing these challenges [2–5]. The demands from various applications have driven prominent developments in NTE systems, encompassing a wide range of chemical substances such as oxides [6–9], fluorides [10–12], cyanides [13–15], and alloys [16]. This substantial diversification has led to various types of NTE compounds. Simultaneously, the pursuit of discovering new NTE materials contributes to a deeper understanding of NTE mechanisms. These include low-frequency phonon vibrations [17,18], spontaneous volume ferroelectrostriction [19], magnetovolume effects in magnetic compounds [20], charge transfer [21], Mott transition [22,23], size effects [24], and more.

Metal fluorides have emerged as highly promising candidates among these materials, offering new functionalities in NTE due to their notable optical transparency in the infrared spectrum and their ability to be fabricated in ceramic form [25]. Although the number of simple $M^{III}F_3$ compounds with ReO_3 connectivity is limited, numerous $A^{II}B^{IV}F_6$ compositions adopt rocksalt cation-ordered ReO_3-type structures (Fig. 1), exhibiting significantly superior NTE properties compared to $M^{III}F_3$ compounds [26]. For instance, $CaZrF_6$ has been reported to exhibit NTE approximately two to three times that of ScF_3 [10,27] over the temperature range 25–400 K. Their respective space groups are *Pm-3m* and *Fm-3m*. As shown in Fig. 1, the metal atoms and the six surrounding fluorine atoms collectively form octahedra connected through shared corners, leading to the well-ordered ReO_3-type structure in ScF_3 and $CaZrF_6$. These structures exhibit a high degree of similarity, where the octahedra are expected to dynamically rotate out of phase with respect to neighboring units about their average positions, resulting in a volume contraction, while maintaining the cubic structure on average [28]. However, the NTE mechanism in fluorides is still controversial, and the mechanism responsible for the differences in thermal expansion properties remains elusive.

In previous studies, the rigid-unit modes model has been proposed to explain the NTE properties of fluorides [29,30]. In contrast, Hu *et al.* pointed out that the rigid units are not necessary for the occurrence of NTE [31], and the different flexibility of the bond leads to differences in NTE among fluorides [32]. However, this flexibility comparison does not extend to monometallic versus bimetallic fluorides. Hancock *et al.* [27] pointed out that disparities in bimetallic fluorides arise from vibration modes predominantly contributing to NTE, situated at distinct high-symmetry points. Subsequently, Wang *et al.* [33] identified the discrepancy as due to band folding, with the dominant phonon modes for NTE in $CaZrF_6$ being the same as in ScF_3. In 2020, Bird *et al.* [34] observed that the scissoring modes in $CaZrF_6$ exhibit greater amplitude

---

[*] Contact author: qsun@zzu.edu.cn

[†] Contact author: heri@nimte.ac.cn

[‡] Contact author: qilonggao@zzu.edu.cn

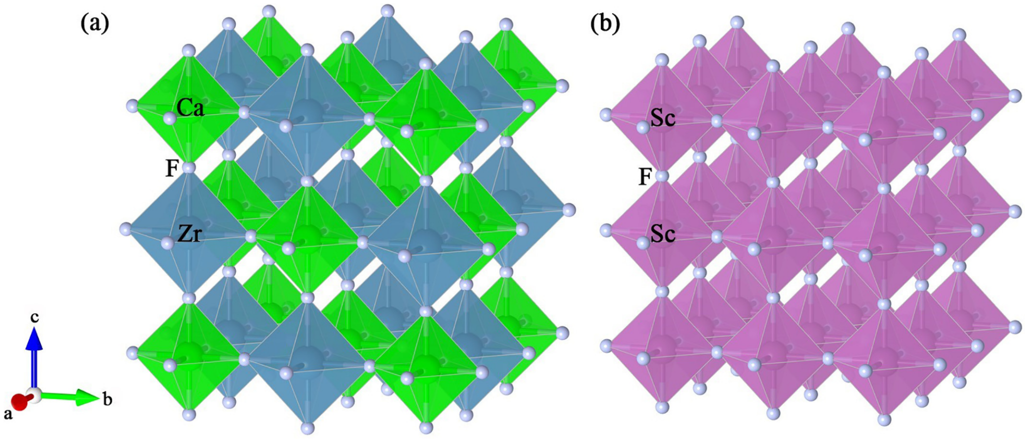

FIG. 1. Crystal structure of (a) $CaZrF_6$ and (b) ScF_3.

compared to those in ScF_3, thus explaining the larger NTE for the former. Despite the above studies having elucidated the difference in NTE between the two substances, none has yet unified the NTE mechanism of monometallic fluoride and bimetallic fluoride. Accordingly, an in-depth study of the underlying mechanism of this difference is needed to establish a coherent relationship between NTE and atomic behavior for systematic materials design.

In this work, we investigated the vibrational differences between $CaZrF_6$ and ScF_3 by employing first-principles calculations and machine-learning deep-potential (DP) methods to analyze in reciprocal and real spaces, respectively. In reciprocal space, we considered the phonons with wave vectors spanning the entire reciprocal space, rather than being confined to dispersion curves along symmetrical directions. Concurrently, we used distortion indices and bond-angle variance to quantify the flexibility, which was verified in real space. The results indicate that the combined effect of vibration modes and polyhedral distortion is the reason for the difference in NTE properties between $CaZrF_6$ and ScF_3.

II. COMPUTATIONAL DETAILS

A. Accurate deep-learning potential

The fundamental idea of the deep-learning potential method involves fitting the energies and atomic forces of various configurations using a deep neural network. Its learning datasets comprise a large number of structural configurations covering a wide range of relevant configurational spaces. Here, we used the DP Generator (DP-GEN) to generate a set of training data. The workflow of each iteration consists of three main steps: training, exploration, and labeling. The training process is described here using $CaZrF_6$ as an example; for detailed information on each step, please refer to the literature [35].

Here, we used DEEPMD-KIT version 2.1.5 [36]. The cutoff radius R_c was set to 6 Å; the sizes of the embedding and fitting networks were (25, 50, 100) and (240, 240, 240), respectively. Additionally, a smoothing potential was applied along with the descriptor [37]. The loss function used in this work has the same form as in the recent study [38]. The weight coefficients for the energy, atomic force, and virial terms in the loss functions change during the optimization process from 0.02 to 1, and from 2000 to 1. The DPs were trained over 700 000 steps, with a learning rate decaying exponentially from 1×10^{-3} to 3.5×10^{-8}. The pressure range was −100–3000 bar and the temperature range was 0–1200 K during training. A model compression scheme was applied to enhance the computational efficiency of the deep-potential molecular dynamics (DPMD) simulation [39]. Additionally, σ_{low} and σ_{high} were set to 0.07 and 0.20 eV/Å, respectively, as suggested in the original literature [40]. The exploration of each system was considered converged when the percentage of accurate configurations exceeded 99%. These hyperparameters have been demonstrated to accurately reproduce the first-principles training database for numerous materials [35–37].

The deep neural network-based DP was trained using the DEEPMD method. We initialized the exploration using a density-functional theory (DFT)-optimized unit cell to capture all characteristic configurations of high-temperature and high-pressure crystal, resulting in the discovery of a total of 29 000 configurations. We compared the energies and atomic forces calculated using the DP model with those obtained from DFT calculations for the configurations in the final training dataset.

As shown in Figs. 2(a) and 2(b), the mean absolute error of energy (ΔE DP-DFT) and atomic force (ΔF DP-DFT) between DP and DFT in $CaZrF_6$ are found to be 2.21 meV per atom and 0.225 meV/Å, respectively. The equilibrium lattice constants of $CaZrF_6$ optimized by DFT and DP are 4.304 and 4.303 Å and the corresponding values of ScF_3 are 4.068 and 4.064 Å, respectively. This is less than 1% error from the experimental values of 4.27 and 4.02 Å. Furthermore, the equations of state of the cubic phase calculated by both DFT and DP are presented in Fig. 2(c). In addition, we utilized the DP model to calculate the phonon-dispersion relations for $CaZrF_6$ and compared them with the DFT calculations. The acoustic branches exist only in the low-frequency region and approach zero frequency towards the high-symmetry Gamma point. The absence of negative phonon frequencies in the dispersion curves indicates the dynamical stability of the material at 0 K and ambient pressure, consistent with the DFT results. However, at low frequencies, there is a discrepancy between the phonon spectra calculated by DFT and DP, which may be that the MD results take into account anharmonicity, as illustrated in Fig. S1 [41–45]. It should be emphasized that

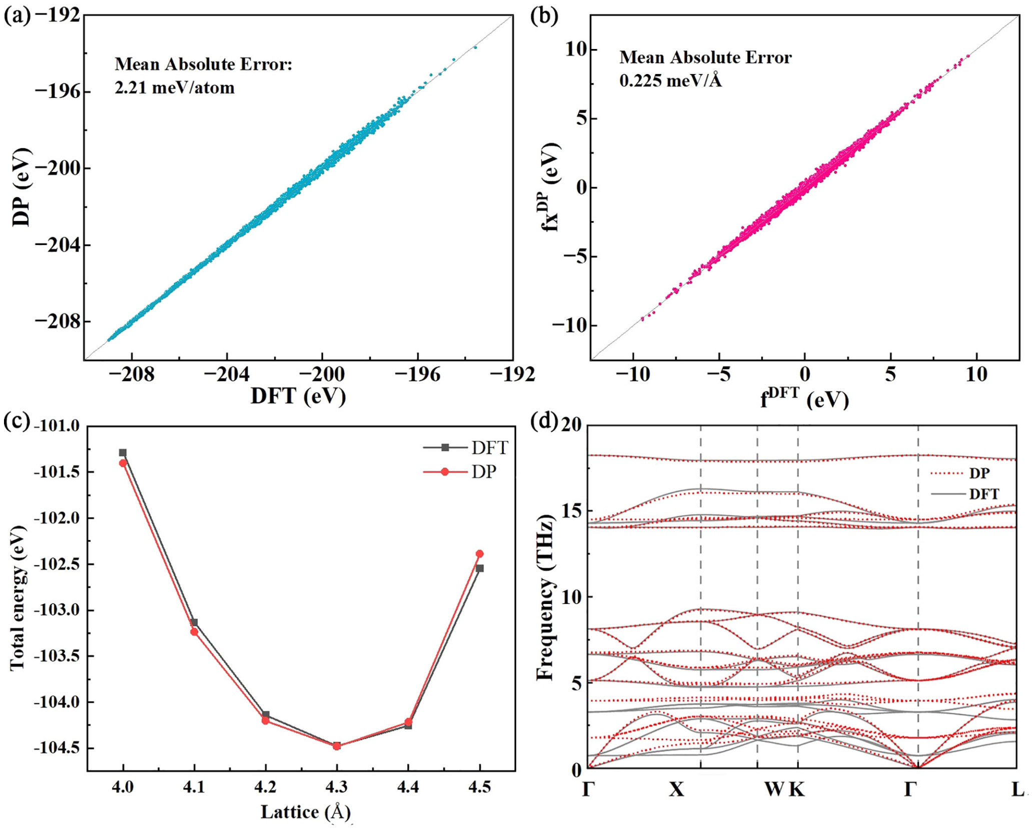

FIG. 2. Benchmark test of DP against DFT results for $CaZrF_6$. Comparison of energies (a) and atomic forces (b) calculated using the DP and DFT for all configurations. DP and DFT energies for different hydrostatic pressure (c) and phonon-dispersion relations (d) for cubic phase.

the phonon spectra are not considered the LO/TO splitting, but this effect is considered (see the results in Fig. 4). For the benchmark test of the ScF_3, see Supplemental Material, Fig. S2 [41]. Our systematic benchmarking shows that the DP achieves excellent DFT-level accuracy and is capable of predicting a range of temperature-dependent properties from first principles.

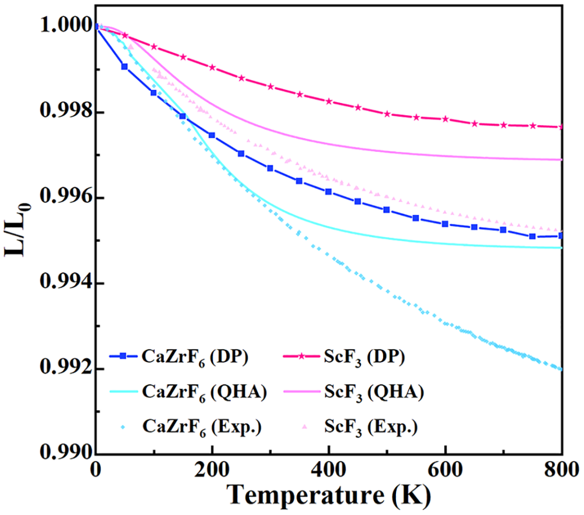

FIG. 3. Relative change of the lattice parameter of $CaZrF_6$ and ScF_3 on heating. The experimental data [10,27], QHA and DP calculations are reported, respectively.

B. DFT calculations

In the first iteration, the initial training dataset was generated by performing a ten-step *ab initio* molecular-dynamics (AIMD) simulation on a randomly perturbed cubic supercell containing 32 atoms at 50 K. To kick off the concurrent learning procedure, an initial training dataset is required. AIMD was performed for producing the atomic structures of the initial training dataset. Subsequently, candidate configurations were identified and labeled, followed by self-consistent DFT calculations. These DFT calculations utilized a plane-wave basis set with a cutoff energy of 500 eV, as implemented in the Vienna *Ab initio* Simulation Package (VASP) [46]. The electron exchange-correlation potential was described using the generalized gradient approximation with the Perdew-Burke-Ernzerhof solid (PBEsol) scheme [47]. For the cubic unit cell, the Brillouin zone was sampled using a 4 × 4 × 4 Monkhorst-Pack *k*-point grid. The DFT calculations were performed at zero pressure. The phonon-dispersion curves considering LO/TO splitting, the Grüneisen parameters, and thermal expansion coefficients were calculated using PHONOPY [48], where the force constants were calculated by finite-difference method employing a 2 × 2 × 2 supercell containing 64 atoms. In the differential calculations, the frequencies at different volumes (±0.2%) of systems were directly used. The

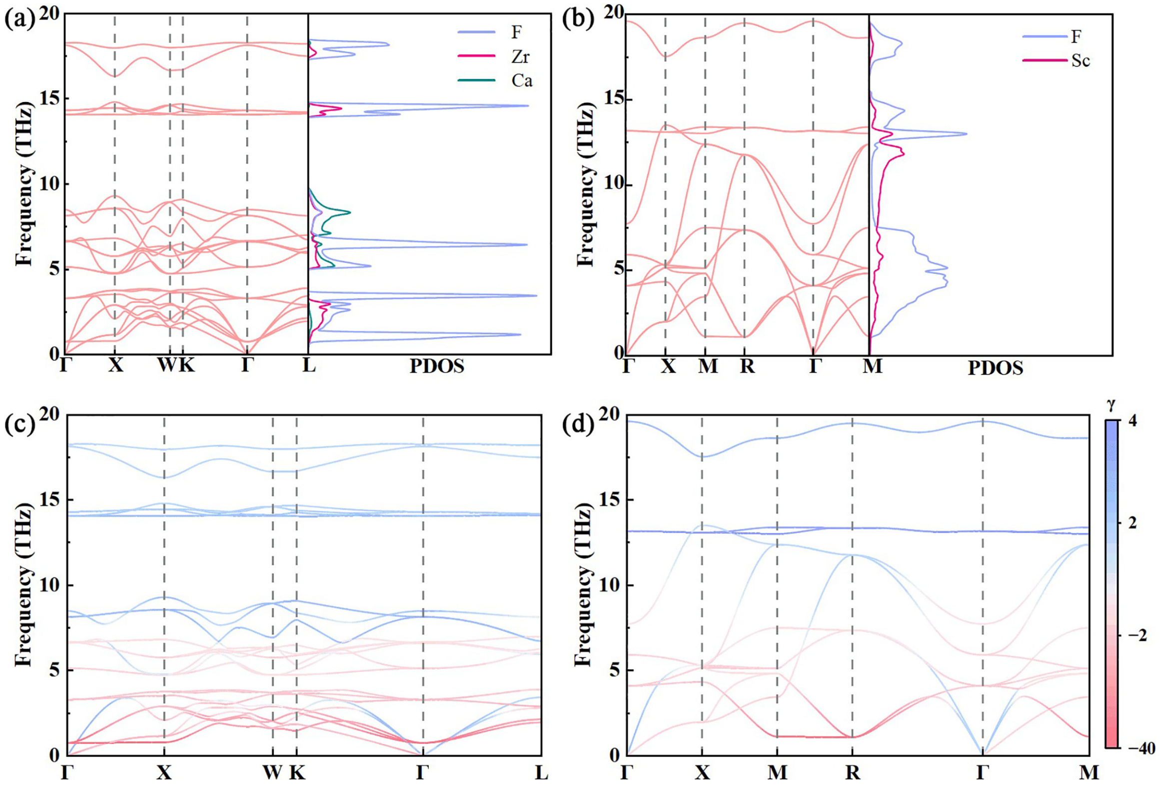

FIG. 4. Phonon-dispersion curves and phonon density of states calculated for (a) $CaZrF_6$ and (b) ScF_3. The phonon dispersion curves are colored according to the values of the corresponding mode Grüneisen parameters γ_i for (c) $CaZrF_6$ and (d) ScF_3.

Grüneisen parameters were calculated by the three-point differential method. The thermal properties of the system were obtained using the quasiharmonic approximation (QHA). In QHA, the volumetric CTE can be obtained from

$$\alpha_V = \frac{1}{B(T)V}\sum_i \gamma_i(T)C_{v_i}(T),$$

where $B(T)$, $\gamma_i(T) = -\partial \ln\omega_i/\partial \ln V$, and C_{Vi} (T) are the bulk modulus, mode Grüneisen parameter, and specific-heat capacity of the ith vibrational mode at temperature T, respectively [49]. Since all modes of $C_{Vi}(T)$ are positive at all temperatures, it is obvious that the positive or negative CTE is only related to the values of mode Grüneisen parameters. The QHA theory contains only implicit anharmonicity (i.e., the volume dependence of phonon frequencies) and ignores explicit anharmonicity (i.e., phonon-phonon anharmonic interactions, which may contribute significantly at high temperature) [50,51]. This approach is generally justified for studies focused on thermal expansion properties of materials at temperatures well below their melting points, as explicit anharmonicity plays a significant role primarily at high temperatures [52–54]. The Helmholtz free energy as a function of volume (F-V) for ten different volumes around the optimized equilibrium volume was fitted using the Vinet equation of states [55], in order to obtain the thermal expansion coefficient.

C. Molecular-dynamics simulations

In the exploration phase, MD simulations were conducted using the LAMMPS code with periodic boundary conditions [56]. These simulations adopted the isobaric-isothermal (*NPT*) ensemble, with the temperature range set from 10 to 1200 K and pressure starting from −100 to 30 000 bar. This range for temperature and pressure exceeds that of the subsequent NTE, ensuring a comprehensive exploratory scope. Temperature control was achieved using a Nosé-Hoover thermostat [57], and the simulation time step was set to 1 fs. All results regarding the NTE of $CaZrF_6$ and ScF_3 were obtained from DPMD simulations. The NTE simulations were performed using an 8 × 8 × 8 supercell, which were performed using a supercell of cubic unit cell containing 32 atoms. The simulations consisted of an equilibrium run of 50 ps, followed by a production run of 100 ps at a specified temperature. The lattice constant, as well as the true (apparent) bond lengths and angles, were calculated from the average of 200 snapshots taken during the 100 ps of the equilibrium state. Additionally, we tested larger supercells and obtained the same results, as shown in Fig S3 [41].

III. RESULTS AND DISCUSSION

A. Negative thermal expansion

Figure 3 shows the relative lattice constant L/L_0 of cubic $CaZrF_6$ and ScF_3 with increasing temperature, calculated by QHA and DP methods, compared with experimental results. Their average CTEs in the temperature range of 50–800 K were also calculated, as reported in Table I. The temperature dependence of the thermal expansion coefficient and specific lattice parameters are illustrated in Figs. S4 and S5. [41] The NTE intensity of $CaZrF_6$ is about twice that of ScF_3.

TABLE I. Calculated bulk modulus of $CaZrF_6$ and ScF_3, and their average CTE (α_{av}) obtained from experimental data, QHA and DP calculations, in the temperature range 50–800 K.

	B (GPa)	$\alpha_{\text{av-exp}}(\times 10^{-6}\,\text{K}^{-1})$	$\alpha_{\text{av-QHA}}(\times 10^{-6}\,\text{K}^{-1})$	$\alpha_{\text{av-DP}}(\times 10^{-6}\,\text{K}^{-1})$
$CaZrF_6$	57.50	−30.10	−20.13	−15.84
ScF_3	100.78	−17.31	−11.66	−8.57

Despite discrepancies between the calculated and experimental results, both methods qualitatively capture the significant difference in NTE properties between the two substances (below about 300 K). Above 300 K, the explicit anharmonicity may have had a large effect on the calculated results, leading to deviations of the QHA data from the experimental results. This is due to the fact that the QHA only considers implicit anharmonicity [58,59]. Nevertheless, our focus here is solely on low temperatures (about below 300 K). To obtain an accurate description of thermal expansion, it is necessary to incorporate higher-order anharmonic terms. Therefore, we utilized DFT data to train the potential function and employ DPMD to calculate the change in lattice constant with temperature. The simulation data further support the differences in NTE, which align with the previous AIMD simulations based on Goedecker-Teter-Hutter pseudopotentials [Fig S1(a)] [41,60].It can be seen that the MD simulations may give good results in high-temperature ranges (above ∼300 K) due to the two types of anharmonicity: (i) explicit anharmonicity, and (ii) implicit anharmonicity included in the MD simulations. But, the zero-point vibration (nuclear quantum effect) [61] is not considered in the MD (DPMD and AIMD) simulations, which may cause the discrepancies between MD and experiment results. Despite the discrepancies with experimental results, our method remains applicable for large-scale atomic simulations, thereby offering support for subsequent material simulations.

B. Local vibration of atoms in reciprocal and real spaces

To delve further into the reasons behind the discrepancy in thermal expansion properties, the phonon-dispersion curves and the density of vibrational states for ScF_3 and $CaZrF_6$ were calculated, as shown in Figs. 4(a) and 4(b). The absence of imaginary frequencies indicates the dynamic stability of both compounds' structures. They are in general agreement with previous calculations. Some of the differences between our calculations and those of Gupta *et al.* may arise from the LO/TO splitting [29,33]. Additionally, the phonon-dispersion curves are colored according to the corresponding Grüneisen parameters (γ_i) to visually identify the contribution of vibration modes to NTE, with deeper red indicating a greater contribution, as depicted in Figs. 4(c) and 4(d). In both compounds, there are minimal vibrations for the metal atoms at high frequencies, particularly evident in ScF_3 where vibrations above about 14 THz are nearly absent for the metal Sc atoms. The metal Zr atoms in $CaZrF_6$ exhibit vibrations equally distributed even at high frequencies, encompassing the entire frequency range. More importantly, the vibrations of Zr atoms contribute to a reduction in Grüneisen's value, indicating their involvement in NTE. Similar conclusions can be drawn for Ca atoms as well. These findings have also been mentioned in previous studies [62], but our calculations more intuitively visualize the contribution of the NTE. Additionally, the separation between the higher and lower parts of the F atom vibrations, especially for $CaZrF_6$, suggests a larger anisotropy between transverse and longitudinal vibrations of the F atoms, potentially contributing to the higher NTE observed in $CaZrF_6$ than in ScF_3. Finally, the steeper slopes of the longitudinal and transverse acoustic branches along the Γ-X paths in ScF_3 indicate its greater stiffness compared to $CaZrF_6$, consistent with the volume modulus calculations presented in Table I.

It is the difference in atomic vibrations that is the root cause of NTE differences. Therefore, we use different methods to deeply explore the vibrations of local atoms in real space and reciprocal spaces. In DPMD simulations, each atom at r_i vibrates about its mean position $\langle r_i\rangle$. The atomic distance between two atoms can thus take an "apparent" value $R = |\langle r_i\rangle - \langle r_j\rangle|$, which is the difference between their average positions, and a time-dependent "true" value defined as the average of the instantaneous difference $r = \langle |r_i - r_j|\rangle$ [40]. The former defines the lattice constants, does not included information on the atomic correlation, and can be directly determined by x-ray- or neutron-diffraction measurements. The latter involves atomic correlation and can be experimentally measured through high-quality x-ray absorption measurements. The difference between apparent and true bond lengths is directly related to the transverse atomic vibrations [63]. Here, the results of calculating the apparent and true M–*F* bond lengths and *M*–F–*M* angles (M = Sc, Ca, Zr) at different temperatures using DPMD are shown in Figs. 5(a) and 5(b). The results for Sc−F are in good agreement with the available experimental data [31], which gives confidence in the reliability of our calculations.

The true bond lengths of *M–F* (M = Sc, Ca, Zr) all show positive thermal expansion, with amplitudes in the order Ca−F > Sc−F > Zr−F, while the apparent bond lengths show almost zero or negative thermal expansion. In considering the relative thermal expansions of the various bonds, we can state that the Sc−F bond in ScF_3 is relatively stiff, the Ca−F bond in $CaZrF_6$ is more flexible, and the Zr−F bond appears to be the stiffest. However, what is interesting is that the apparent bond length of Ca−F shrinks significantly, while the Zr-F bond in $CaZrF_6$ and the Sc−F bond in ScF_3 did not change significantly. This is one of the reasons for the NTE difference between $CaZrF_6$ and ScF_3. Moreover, Zr^{4+} has a larger positive charge than Ca^{2+}, which means that the F atom is not in the middle of the Ca−F−Zr linkage. The uneven stress on both sides of the F atom makes it easier for the F atom to vibrate. Accordingly, it can be observed that the average of the true *M*–F–*M* angle (M = Sc, Ca, Zr), calculated from the time evolution of the *M*–F–*M* angle of the true bond distances, deviates from 180 ° with temperature, and the

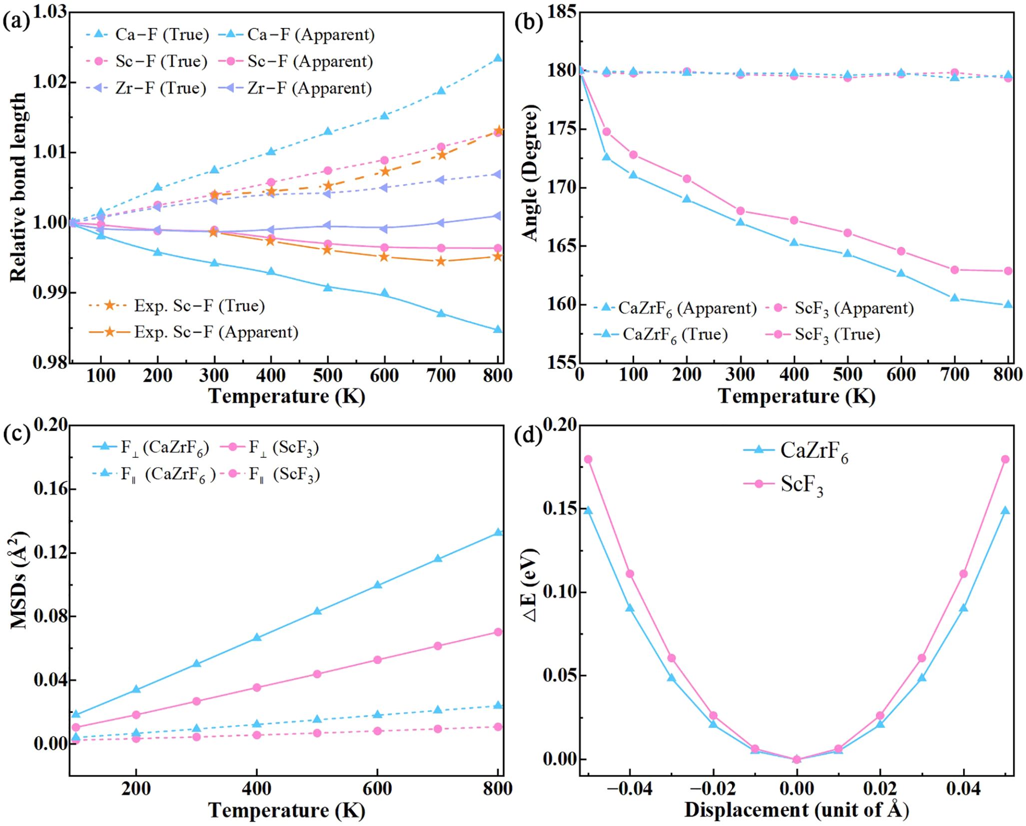

FIG. 5. Calculated true and apparent bond lengths of (a) M–F (M = Sc, Ca, Zr) and true and apparent angle of (b) M–F–M bonds as a function of temperature. For comparison, the experimental Sc–F bond lengths are also reported [31]. (c) Temperature dependence of perpendicular (⊥) and parallel (‖) MSDs of F atoms. (d) Potential well of F atoms moving transversely in $CaZrF_6$ and ScF_3.

amplitude of this deviation is larger for $CaZrF_6$ than for ScF_3, even though their apparent bond length is obviously constant at 180 °.

The contribution of transverse vibrations of nonmetallic atoms is known to contribute significantly to NTE [62,64]. It is clear from the phonon curves in Fig. 4 that the vibrations of F atoms make an important contribution to NTE. The anisotropic mean-square displacements (MSDs) of F atoms are subsequently calculated, the ones most involved in the transverse vibrations of the M–F–M bonds, contributed by phonons in the entire Brillouin zone [Fig. 5(c)]. As expected, it can be observed that the MSDs correlate well with the thermal expansion behavior in both compounds. The anisotropy of $CaZrF_6$ is greater than that of ScF_3, and the amplitude of vibrations of $CaZrF_6$ is about twice that of ScF_3. This finding is also consistent with the calculated results of phonon spectra reported in Fig. 4 and with the relative discussion given above. As shown in Fig. 5(c), the transverse vibrations of both ScF_3 and $CaZrF_6$ exceed the longitudinal ones, and so the arrangement of the bimetals facilitates the vibrations of the F atoms. Then, the potential well of F atoms was calculated by moving F transversely to assess the change in the bond strength of M–F and to elucidate the reason for the transverse vibration difference of F in the two systems. The total energy of the systems at the equilibrium positions was set to zero. As depicted in Fig. 5(d), the potential well becomes flatter from ScF_3 to $CaZrF_6$, indicating that the F atom in $CaZrF_6$ is more prone to vibration.

C. Phonon-mode vibrations

In the quasiharmonic approximation, the contribution of different phonon modes to thermal expansion depends on the positive or negative value of the corresponding mode Grüneisen parameter: the larger the negative value of the mode Grüneisen parameter, the stronger the contribution to the NTE. To obtain more detailed information, we have extracted the Grüneisen parameters of all phonon modes within a 30 × 30 × 30 grid in the Brillouin zone, as shown in Figs. 6(a) and 6(b). A large number of phonon modes near 0–2 THz in both systems exhibit negative Grüneisen parameters. However, $CaZrF_6$ shows larger values and a greater number of negative Grüneisen parameters compared to ScF_3, resulting in a much larger NTE effect in $CaZrF_6$ than in ScF_3. As suggested by Figs. 6(a) and 6(b), the higher-frequency modes predominantly have positive-mode Grüneisen parameters. Notably, there is a sharp distribution of negative-mode Grüneisen parameters for mode frequencies up to about 1 THz. The number of vibration modes with negative Grüneisen parameters is comparable to those with positive Grüneisen parameters, and this widespread presence of vibrational modes with negative Grüneisen parameters (in particular below ∼2 THz) leads to an overall NTE in both materials.

Further insights into NTE can be obtained through the analysis of the eigenvectors of the vibrational modes and structural flexibility. In Figs. 6(a) and 6(b), inside the dotted boxes, we observe all vibrational modes with frequencies below 2 THz and Grüneisen parameters less than −10. We selected

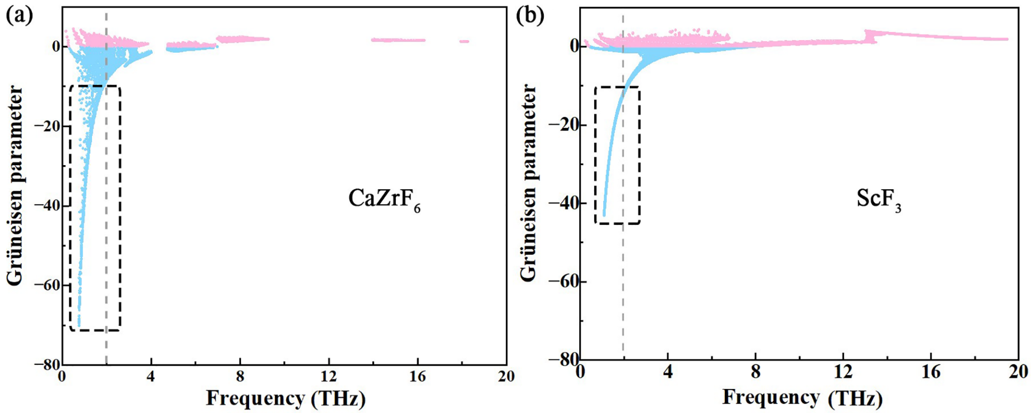

FIG. 6. Grüneisen parameters plotted as a function of the vibrational frequency in (a) $CaZrF_6$ and (b) ScF_3.

some vibrational modes in this window, as shown in Fig. S6 [41]. It can be found that many of these vibrational modes primarily involve the tilt distortion of the octahedra and the tilt vibration depicted (see Fig. 8), which narrow the distance between metal atoms and contribute to NTE. In addition, as the vibration frequency increases (below 2 THz), the metal atoms also begin to vibrate. In ScF_3, the vibrations of metal atoms are mainly reflected in mode 3 (see Fig. S6), while in $CaZrF_6$, the tilt vibration of the octahedron is accompanied by the vibration of metal atoms, in addition to the vibration of metal atoms in mode 3. Of these, the vibration directions of Ca and Zr are almost opposite (Fig. S6), contributing to NTE as well. However, because the vibration of metal atoms requires more energy, the Grüneisen parameter is relatively small. Therefore, it can be established that these tilt vibrations lead to the production of NTE, with a greater contribution in $CaZrF_6$ due to the mixed ordering of metal atoms. Interestingly, the vibration frequencies of ScF_3 are higher than those of $CaZrF_6$ for the same vibration modes, and the negative values of the Grüneisen parameters are weaker, corresponding to a reduced NTE. This significant difference in Grüneisen parameters for the same vibrational modes begs the question: Why?

The bond-angle variance and quadratic elongation have been used to describe the distortion of octahedra, and it has been proven that the distortion of the crystal structure is related to the lattice volume [65]. Inspired by this, we explored the structural flexibility of $CaZrF_6$ and ScF_3 through the distortion index and bond-angle variance of the metal octahedra, which represent the distortion of bond length and bond angle, respectively. A distortion index, D, based on bond lengths, was defined by Baur [66] as

$$D = \frac{1}{n}\sum_{i=1}^{n}\frac{|l_i - l_{\mathrm{av}}|}{l_{\mathrm{av}}},$$

where l_i is the distance from the central atom to the ith coordinating atom, and l_{av} is the average bond length. The bond-angle variance, σ^2 [67], is calculated only for tetrahedra, octahedra, cubes, dodecahedra, and icosahedra:

$$\sigma^2 = \frac{1}{m-1}\sum_{i=1}^{m}(\phi_i - \phi_0)^2,$$

where m is the number of faces in the polyhedron multiplied by 3/2 (i.e., the number of bond angles), ϕ_i is the ith bond angle, and ϕ_0 is the ideal bond angle for a regular polyhedron (for example, 109.47° for a regular octahedra with equal edges).

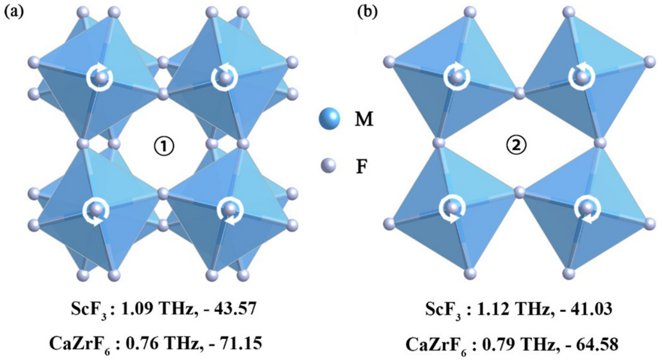

FIG. 7. Selected (a) vibrational mode 1 and (b) mode 2 with the most negative Grüneisen parameters in ScF_3 and $CaZrF_6$. M in the figure is Ca, Sc, Zr.

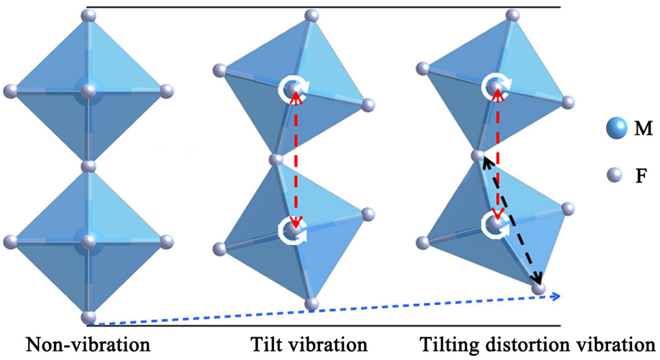

FIG. 8. The left sketch depicts the ideal octahedral connection model, the middle sketch illustrates the vibrational mode with only the contribution of tilt vibration, and the right one shows the mode with the combined action of the tilt vibrational mode and the octahedral distortion. The red arrows indicate the distances between metal atoms, which decrease under tilt vibration, and the black arrows are the distances between F atoms, which decrease during distortion. M in the figure is Ca, Sc, Zr.

TABLE II. Calculated distortion index and bond-angle variance in $CaZrF_6$ and ScF_3 of two selected vibration modes with the largest negative Grüneisen parameters.

	ScF_3		$CaZrF_6$			
	D_{ScF6}	σ^2_{ScF6}	D_{CaF6}	σ^2_{CaF6}	D_{ZrF6}	σ^2_{ZrF6}
Mode 1	0.012	0.089	0.024	21.157	0.02	17.505
Mode 2	0.008	0.533	0.011	18.259	0.009	14.556

We selected the two vibrations that contribute the most to NTE. The two vibration modes are tilt vibrations, in which mode 1 is the antiphase vibration of octahedra between adjacent surfaces, and mode 2 is the simultaneous vibration between adjacent octahedra layers. Both vibrational modes contribute to $CaZrF_6$ and ScF_3, but the Grüneisen parameter of $CaZrF_6$ is about twice that of ScF_3 under the same vibration mode (Fig. 7). Therefore, their metal octahedral distortion index and bond-angle variance are extracted, as shown in Table II. It can be observed that the distortion index and the bond-angle variation are generally larger for the CaF_6 and ZrF_6 octahedra in $CaZrF_6$ than for the ScF_6 octahedra in ScF_3.

Based on these results, we can attribute the fundamental difference in thermal expansion between the two fluorides to the combined effect of tilt vibration and octahedral distortion, as illustrated in Fig. 8. In ScF_3, the ScF_6 octahedra experience modest distortion, resulting in a smaller contribution to NTE from polyhedral distortion. The transverse vibrations of F atoms, coupled with the tilt vibration of ScF_6 octahedra, decrease the Sc−Sc distance. Conversely, in the case of $CaZrF_6$, besides the contribution from tilt vibration, octahedral distortion makes a greater contribution to NTE (tilt-distorted vibrations). The arrangement of the two metal atoms induces distortion of the polyhedra (depicted by the black arrow), further enhancing NTE.

In reciprocal space, we extracted some vibrational modes that contribute significantly to the NTE, while the contribution of all vibrational modes will be reflected in the vibrations in real space. To further validate our results and verify the influence of octahedral distortion on NTE, the distortion of metal octahedra in real space with temperature was simulated using DPMD (Fig. 9), and the findings are consistent with the DFT results. In Fig. 9(a), the distortion of bond length intensifies with increasing temperature, and the ascending amplitude follows the order $CaF_6 > ScF_6 > ZrF_6$, in line with the respective bond strengths of the *M*–F bonds found above. The same trend holds for the distortion of polyhedral bond angles. The degree of distortion in the CaF_6 octahedra exceeds that of both ScF_6 and ZrF_6 by a considerable margin, resulting in the NTE of $CaZrF_6$ being greater than that of ScF_3.

IV. CONCLUSION

In this study, in order to explore the reasons for the differences in thermal expansion properties between $CaZrF_6$ and ScF_3 in detail, and in line with existing perspectives, we aimed to comprehensively compare the thermal vibrations of the two substances. We explored alterations induced by variations in metal atoms to identify differences between their vibrational modes and uncover the underlying mechanism behind the different NTE. Therefore, we discussed the local vibrations of atoms from two perspectives: reciprocal space and real space. In real space, the variation of “true” bond length and bond angle with temperature reflects the flexibility of the bond: Ca−F > Sc−F > Zr−F. The vibrations amplitude of F atoms in $CaZrF_6$ exceeds that of ScF_3, while changes in apparent bond length and angle provide clearer insight into the significant contribution of the Ca−F bond to NTE. Different *M* metal atoms lead to a more pronounced decrease in the *M*–F–*M* angle of $CaZrF_6$ compared to ScF_3, resulting in a larger shrink between the metal atoms in $CaZrF_6$.

In reciprocal space, besides the bond flexibility between the two substances, it is crucial to gain a more intuitive understanding of the contribution of low-frequency phonon vibrations to NTE. Upon investigating the local vibrations of $CaZrF_6$ and ScF_3 across the entire reciprocal space, we observed that $CaZrF_6$ exhibits a greater number of vibration modes contributing to NTE than ScF_3, attributed to the change in flexibility induced by the presence of two metal atoms. A more comprehensive inquiry revealed that the extent of distortion experienced by the tilted octahedra during

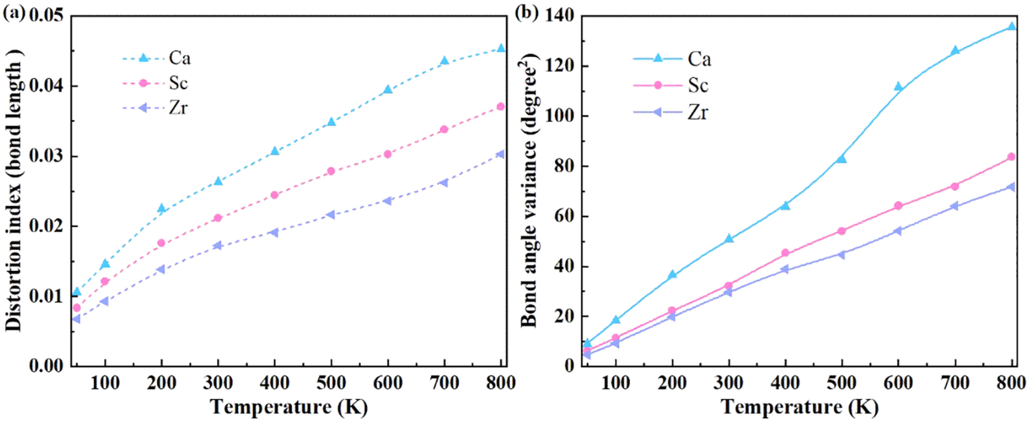

FIG. 9. (a) The variation of octahedral distortion index and (b) the bond-angle variance of CaF_6, ScF_6, and ZrF_6 polyhedra with temperature.

the vibration process varies. Specifically, $CaZrF_6$ exhibits a greater degree of distortion compared to ScF_3, a discrepancy that evidently arises as a direct consequence of bond flexibility.

To validate our calculation results, we also verified them in real space by DPMD simulations, and the results were consistent with those in reciprocal space. Hence, the fundamental difference in thermal expansion between the two fluorides is the combined result of tilt vibrations and octahedral distortions. The ordered arrangement of the two metal atoms intertwines vibrational modes, leading to the presence of more vibration modes contributing to NTE in $CaZrF_6$ than in ScF_3, with the roles of Ca and Zr being indispensable in this regard. Moreover, the substantial distortion of the octahedra in $CaZrF_6$ further enhances NTE. Our results provide valuable implications for large-scale simulation and adjustment of NTE in fluoride materials.

ACKNOWLEDGMENTS

This work was supported by the National Natural Science Foundation of China (Grants No. 22071221, No. 21905252, No. 12374032, and No. 12204496), and Natural Science Foundation of Henan Province (Grants No. 222301420040 and No. 242300421376), and the Zhejiang Provincial Natural Science Foundation (Grant No. Q23A040003). Special thanks to Martin. T. Dove of Queen Mary University of London for helpful discussions. All calculations were performed with the support of the National Supercomputing Center in Zhengzhou.

---

[1] O. Sigmund and S. Torquato, Composites with extremal thermal expansion coefficients, Appl. Phys. Lett. **69**, 3203 (1996).

[2] G. D. Barrera, J. A. O. Bruno, T. H. K. Barron, and N. L. Allan, Topical review: Negative thermal expansion, J. Phys.: Condens. Matter **17**, 217 (2005).

[3] T. Koshi, Negative thermal expansion materials: Technological key for control of thermal expansion, Sci. Technol. Adv. Mater. **13**, 013001 (2016).

[4] M. T. Dove and H. Fang, Negative thermal expansion and associated anomalous physical properties: Review of the lattice dynamics theoretical foundation, Rep. Prog. Phys. Phys. Soc. **79**, 066503 (2016).

[5] E. Liang, Q. Sun, H. Yuan, J. Wang, G. Zeng, and Q. Gao, Negative thermal expansion: Mechanisms and materials, Front. Phys. **16**, 53302 (2021).

[6] T. A. Mary, J. S. O. Evans, T. Vogt, and A. Sleight, Negative thermal expansion from 0.3 to 1050 Kelvin in ZrW_2O_8, Science **272**, 90 (1996).

[7] X. Zhen, A. Sanson, Q. Sun, E. Liang, and Q. Gao, Role of alkali ions in the near-zero thermal expansion of NaSICON-type $AZr_2(PO_4)_3$ (A = Na, K, Rb, Cs) and $Zr_2(PO_4)_3$ compounds, Phys. Rev. B **108**, 144102 (2023).

[8] F. Alabarse, B. Baptiste, B. Joseph, and J. Haines, Tuning negative thermal expansion in $AlPO_4$-17 by insertion of guest molecules, J. Phys. Chem. Lett. **13**, 9390 (2022).

[9] W. Wei, Q. Gao, J. Guo, M. Chao, L. He, J. Chen, and E. Liang, Realizing isotropic negative thermal expansion covering room temperature by breaking the superstructure of ZrV_2O_7, Appl. Phys. Lett. **116**, 181902 (2020).

[10] Q. Gao, S. Zhang, Y. Jiao, Y. Qiao, A. Sanson, Q. Sun, X. Shi, E. Liang, and J. Chen, A new isotropic negative thermal expansion material of $CaSnF_6$ with facile and low-cost synthesis, Nano Res. **16**, 5964 (2023).

[11] B. K. Greve, K. L. Martin, P. L. Lee, P. J. Chupas, K. W. Chapman, and A. P. Wilkinson, Pronounced negative thermal expansion from a simple structure: Cubic ScF_3, J. Am. Chem. Soc. **132**, 15496 (2010).

[12] Y. Qiao, S. Zhang, P. Zhang, J. Guo, A. Sanson, X. Zhen, and J. Chen, Simple chemical synthesis and isotropic negative thermal expansion in $MHfF_6$ (M = Ca, Mn, Fe, and Co), Nano Res. **17**, 2195 (2024).

[13] S. d'Ambrumenil, M. Zbiri, S. J. Hibble, A. M. Chippindale, D. S. Keeble, C. Wright, and N. H. Rees, Anomalous thermal expansion in one-dimensional transition metal cyanides: Behavior of the trimetallic cyanide $Cu_{1/3}Ag_{1/3}Au_{1/3}CN$, Phys. Rev. B **100**, 174302 (2019).

[14] Q. Gao, Y. Jiao, Q. Sun, J. A. Sprenger, M. Finze, A. Sanson, and J. Chen, Giant negative thermal expansion in ultralight $NaB(CN)_4$, Angew. Chem. Int. Ed. **63**, e202401302 (2024).

[15] J. Wang, Q. Gao, Y. Gao, Y. Luo, J. Guo, Q. Sun, and E. Liang, Uniaxial negative thermal expansion behavior of β-CuSCN, Appl. Phys. Lett. **118**, 222105 (2021).

[16] X. Yuan, B. Wang, Y. Sun, H. Guo, K. Shi, S. Deng, L. He, H. Lu, H. Zhang, S. Xu, Y. Du, S. Chu, W. Hao, and C. Wang, High-entropy anti-perovskites with enhanced negative thermal expansion behavior, Adv. Funct. Mater. 2404629 (2024).

[17] V. Gava, A. L. Martinotto, and C. A. Perottoni, First-principles mode Gruneisen parameters and negative thermal expansion in α-ZrW_2O_8, Phys. Rev. Lett. **109**, 195503 (2012).

[18] R. Mittal, M. K. Gupta, and S. L. Chaplot, Phonons and anomalous thermal expansion behavior in crystalline solids, Prog. Mater Sci. **92**, 360 (2018).

[19] Z. Pan, Y. W. Fang, T. Nishikubo, L. Hu, S. Kawaguchi, and M. Azuma, Tolerance factor control of tetragonality and negative thermal expansion in $PbTiO_3$-based ferroelectrics, Chem. Mater. **34**, 2798 (2022).

[20] K. Takenaka and H. Takagi, Giant negative thermal expansion in Ge-doped anti-perovskite manganese nitrides, Appl. Phys. Lett. **87**, 261902 (2005).

[21] Y. W. Long, N. Hayashi, T. Saito, M. Azuma, S. Muranaka, and Y. Shimakawa, Temperature-induced A–B intersite charge transfer in an A-site-ordered $LaCu_3Fe_4O_{12}$ perovskite, Nature (London) **458**, 60 (2009).

[22] K. Takenaka, Y. Okamoto, T. Shinoda, N. Katayama, and Y. Sakai, Colossal negative thermal expansion in reduced layered ruthenate, Nat. Commun. **8**, 14102 (2017).

[23] S. Xu, Y. Hu, Y. Liang, C. Shi, Y. Su, J. Guo, Q. Gao M. Chao, and E. Liang, Negative thermal expansion of Ca_2RuO_4 with oxygen vacancies, Chin. Phys. B **29**, 086501 (2020).

[24] X. Song, Z. Sun, Q. Huang, M. Rettenmayr, X. Liu, M. Seyring, G. Li, G. Rao, and F. Yin, Adjustable zero thermal expansion in antiperovskite manganese nitride, Adv. Mater. **23**, 4690 (2011).

[25] V. Nazabal, M. Poulain, M. Olivier, P. Pirasteh, P. Camy, J.-L. Doualan, S. Guy, T. Djouama, A. Boutarfaia, and J. L. Adam, Fluoride and oxyfluoride glasses for optical applications, J. Fluorine Chem. **134**, 18 (2012).

[26] H. Ueda, T. Inamori, A. Taguchi, C. Michioka, and K. Yoshimura, Systematic studies on magnetism of divalent 3d transition metal ions in ordered ReO_3-type fluorides MZrF$_6$ ($M =$ Ti, V, Cr, Mn, Fe, Co, Ni, and Cu), J. Phys. Soc. Jpn. **91**, 014704 (2022).

[27] J. C. Hancock, K. W. Chapman, G. J. Halder, C. R. Morelock, B. S. Kaplan, L. C. Gallington, A. Bongiorno, C. Han, S. Zhou, and A. P. Wilkinson, Large negative thermal expansion and anomalous behavior on compression in cubic ReO_3-Type $A^{II}B^{IV}F_6$:CaZrF$_6$ and CaHfF$_6$, Chem. Mater. **27**, 3912 (2015).

[28] T. Chatterji, P. F. Henry, R. Mittal, and S. L. Chaplot, Negative thermal expansion of ReO_3: Neutron diffraction experiments and dynamical lattice calculations, Phys. Rev. B. **78**, 134105 (2008).

[29] M. T. Dove, Z. Wei, A. E. Phillips, D. A. Keen, and K. Refson, Which phonons contribute most to negative thermal expansion in ScF_3?, APL Mater. **11**, 041130 (2023).

[30] C. Wang, L. Wang, Y. Sun, K. Shi, H. Lu S.Deng, and P. Hu, X. Zhang, Metal fluorides, a new family of negative thermal expansion materials, J. Materiomics **1**, 106(2015).

[31] L. Hu, J. Chen, A. Sanson, H. Wu, C. G. Rodriguez, L. Olivi, Y. Ren, L. Fan, J. Deng, and X. Xing, New insights into the negative thermal expansion: Direct experimental evidence for the "Guitar-String" effect in cubic ScF_3, J. Am. Chem. Soc. **27**, 8320 (2016).

[32] L. Hu, J. Chen, J. Xu, N. Wang, F. Han, Y. Ren, Z. Pan, Y. Rong, R. Huang, J. Deng, L. Li, and X. Xing, Atomic linkage flexibility tuned isotropic negative, zero, and positive thermal expansion in MZrF$_6$ ($M =$ Ca, Mn, Fe, Co, Ni, and Zn), J. Am. Chem. Soc. **138**, 14530 (2016).

[33] N. Wang, J. Deng, J. Chen, and X. Xing, Phonon spectrum attributes for the negative thermal expansion of MZrF$_6$ ($M =$ Ca, Mn–Ni, Zn), Inorg. Chem. Front. **6**, 1022 (2019).

[34] T. A. Bird, J. Woodland-Scott, L. Hu, M. T. Wharmby, J. Chen, A. L. Goodwin, and M. S. Senn, Anharmonicity and scissoring modes in the negative thermal expansion materials ScF_3 and CaZrF$_6$, Phys. Rev. B. **101**, 064306 (2020).

[35] Y. Zhang, H. Wang, W. Chen, J. Zeng, L. Zhang, H. Wang, and E. W., DP-GEN: A concurrent learning platform for the generation of reliable deep learning based potential energy models, Comput. Phys. Commun. **253**, 107206 (2020).

[36] J. Z. Zeng, D. Zhang, D. H. Lu, P. H. Mo, Z. Y. Li, Y. X. Chen, M. Rynik, L. Huang, Z. Y. Li, S. C. Shi, Y. Z. Wang, H. T. Ye, P. Tuo, J. B. Yang, Y. Ding, Y. F. Li, D. Tisi, Q. Y. Zeng, H. Bao, Y. Xia *et al.*, DeePMD-kit v2: A software package for deep potential models, J. Chem. Phys. **159**, 054801 (2023).

[37] L. F. Zhang and J. Q. Han, Deep potential molecular dynamics: A scalable model with the accuracy of quantum mechanics, Phys. Rev. Lett. **120**, 143001 (2018).

[38] R. He, H. Wu, L. Zhang, X. Wang, F. Fu, S. Liu, and Z. Zhong, Structural phase transitions in $SrTiO_3$ from deep potential molecular dynamics, Phys. Rev. B **105**, 064104 (2022).

[39] D. Lu, W. Jiang, Y. Chen, L. Zhang, W. Jia, H. Wang, and M. Chen, DP Compress: A model compression scheme for generating efficient deep potential models, J. Chem. Theory Comput. **18**, 5559 (2022).

[40] R. He, H. Wu, Y. Lu, and Z. Zhong, Origin of negative thermal expansion and pressure-induced amorphization in zirconium tungstate from a machine-learning potential, Phys. Rev. B **106**, 174101 (2022).

[41] See Supplemental Material at http://link.aps.org/supplemental/10.1103/PhysRevB.110.064322 for the anharmonicity. It also contains Refs. [11,27,34,42–45,50,51,60,61].

[42] A. Togo, L. Chaput, I. Tanaka, and G. Hug, First-principles phonon calculations of thermal expansion in Ti_3SiC_2, Ti_3AlC_2, and Ti_3GeC_2, Phys. Rev. B **81**, 174301 (2010).

[43] C. W. Li, J. Ma, H. B. Cao, A. F. May, D. L. Abernathy, G. Ehlers, C. Hoffmann, X. Wang, T. Hong, A. Huq, O. Gourdon, and O. Delaire, Anharmonicity and atomic distribution of SnTe and PbTe thermoelectrics, Phys. Rev. B. **90**, 214303 (2014).

[44] P. Lazar, T. Bucko, and J. Hafner, Negative thermal expansion of ScF_3: Insights from density-functional molecular dynamics in the isothermal-isobaric ensemble, Phys. Rev. B **92**, 224302 (2015).

[45] H. E. Sauceda, V. Vassilev-Galindo, S. Chmiela, K. Müller, and Al. Tkatchenko, Dynamical strengthening of covalent and non-covalent molecular interactions by nuclear quantum effects at finite temperature, Nat. Commun. **12**, 442 (2021).

[46] G. Kresse and J. Furthmüller, Efficient iterative schemes for ab initio total-energy calculations using a plane-wave basis set, Phys. Rev. B **54**, 11169 (1996).

[47] J. P. Perdew, K. Burke, and M. Ernzerhof, Generalized gradient approximation made simple, Phys. Rev. Lett. **78**, 1396(E) (1997).

[48] A. Togo, F. Oba, and I. Tanaka, First-principles calculations of the ferroelastic transition between rutile-type and $CaCl_2$-type SiO_2 at high pressures, Phys. Rev. B **78**, 134106 (2008).

[49] J. W. Zwanziger, Phonon dispersion and Grüneisen parameters of zinc dicyanide and cadmium dicyanide from first principles: Origin of negative thermal expansion, Phys. Rev. B **76**, 052102 (2007).

[50] O. Hellman, I. A. Abrikosov, and S. I. Simak, Lattice dynamics of anharmonic solids from first principles, Phys. Rev. B **84**, 180301(R) (2011).

[51] O. Hellman, P. Steneteg, I. A. Abrikosov, and S. I. Simak, Temperature dependent effective potential method for accurate free energy calculations of solids, Phys. Rev. B **87**, 104111 (2013).

[52] S. d'Ambrumenil, M. Zbiri, A. M. Chippindale, and S. J. Hibble, Phonon dynamics in the layered negative thermal expansion compounds CuxNi$_{2-x}$(CN)$_4$, Phys. Rev. B **100**, 094312 (2019).

[53] L. H. N. Rimmer, M. T. Dove, B. Winkler, D. J. Wilson, K. Refson, and A. L. Goodwin, Framework flexibility and the negative thermal expansion mechanism of copper(I) oxide Cu_2O, Phys. Rev. B **89**, 214115 (2014).

[54] M. Calleja, A. L. Goodwin, and M. T. Dove, Origin of the colossal positive and negative thermal expansion in $Ag_3[Co(CN)_6]$: An *ab initio* density functional theory study, J. Phys.: Condens. Matter. **20**, 255226 (2008).

[55] P. Vinet, J. H. Rose, J. Ferrante, and J. R. Smith, Universal features of the equation of state of solids, J. Phys.: Condens. Matter. **1**, 1941 (1989).

[56] S. Plimpton, Fast parallel algorithms for short-range molecular dynamics, J. Comput. Phys. 117, 1 (1995).

[57] S. Nosé, A unified formulation of the constant temperature molecular dynamics methods, J. Chem. Phys. **81**, 511 (1984).

[58] P. B. Allen, Anharmonic phonon quasiparticle theory of zero-point and thermal shifts in insulators: Heat capacity, bulk modulus, and thermal expansion, Phys. Rev. B **92**, 064106 (2015).

[59] K. Kamali, T. R. Ravindran, C. Ravi, Y. Sorb, N. Subramanian, and A. K. Arora, Anharmonic phonons of $NaZr_2(PO_4)_3$ studied by Raman spectroscopy, first-principles calculations, and x-ray diffraction, Phys. Rev. B **86**, 144301 (2012).

[60] D. Bocharov, M. Krack, Y. Rafalskij, A. Kuzmin, and J. Purans, Ab initio molecular dynamics simulations of negative thermal expansion in ScF_3: The effect of the supercell size, Comput. Mater. Sci. **171**, 109198 (2020).

[61] H. Y. Wu, R. He, Y. Lu, and Z. Zhong, Large-scale atomistic simulation of quantum effects in $SrTiO_3$ from first principles, Phys. Rev. B **106**, 224102 (2022).

[62] M. K. Gupta, B. Singh, R. Mittal, and S. L. Chaplot, Negative thermal expansion behavior in MZrF$_6$ ($M =$ Ca, Mg, Sr): *Ab initio* lattice dynamical studies, Phys. Rev. B **98**, 014301 (2018).

[63] W. Miller, C. W. Smith, D. S. Mackenzie, and K. E. Evans, Negative thermal expansion: A review, J. Mater. Sci. **44**, 5441 (2009).

[64] M. K. Gupta, B. Singh, R. Mittal, M. Zbiri, A. B. Cairns, A. L. Goodwin, H. Schober, and S. L. Chaplot, Anomalous thermal expansion, negative linear compressibility, and high-pressure phase transition in $ZnAu_2(CN)_4$: Neutron inelastic scattering and lattice dynamics studies, Phys. Rev. B **96**, 214303 (2017).

[65] R. Uehara, R. Kaneda, T. Takei, N. Kumada, S. Matsushita, A. Nakajima, and T. Isobe, Effect of aliovalent substitution on the crystal distortion and negative thermal expansion properties of $Zr_2SP_2O_{12,}$, Ceram. Int. **49**, 22197 (2023).

[66] W. H. Baur, The geometry of polyhedral distortions. Predictive relationships for the phosphate group, Acta Crystallogr., Sect. B **30**, 1195 (1974).

[67] K. Robinson, G. V. Gibbs, and P. H. Ribbe, Quadratic elongation: A quantitative measure of distortion in coordination polyhedra, Science **172**, 567 (1971).